

Draft version as submitted to Physical Review Special Topics: Accelerators and Beams.

Extension of the Finite Integration Technique including dynamic mesh refinement and its application to self-consistent beam dynamics simulations

Sascha M. Schnepf*

Graduate School of Computational Engineering,

Technische Universität Darmstadt, Dolivostr. 15, 64293 Darmstadt, Germany

Erion Gjonaj[†] and Thomas Weiland[‡]

Institut für Theorie Elektromagnetischer Felder,

TEMF, Technische Universität Darmstadt,

Schloßgartenstr. 8, 64289 Darmstadt, Germany

(Dated: August 26, 2021)

Abstract

An extension of the framework of the Finite Integration Technique (FIT) including dynamic and adaptive mesh refinement is presented. After recalling the standard formulation of the FIT, the proposed mesh adaptation procedure is described. Besides the linear interpolation approach, a novel interpolation technique based on specialized spline functions for approximating the discrete electromagnetic field solution during mesh adaptation is introduced. The standard FIT on a fixed mesh and the new adaptive approach are applied to a simulation test case with known analytical solution. The numerical accuracy of the two methods are shown to be comparable. The dynamic mesh approach is, however, much more efficient. This is also demonstrated for the full scale modeling of the complete RF gun at the Photo Injector Test Facility DESY Zeuthen (PITZ) on a single computer. Results of a detailed design study addressing the effects of individual components of the gun onto the beam emittance using a fully self-consistent approach are presented.

PACS numbers: 02.70.Bf, 29.27.Bd, 41.75.Fr

Keywords: Finite Integration Technique, Adaptive Dynamic Mesh Refinement, Particle-In-Cell

* schnepf@gsc.tu-darmstadt.de; Author to whom any correspondence should be addressed.

[†] gjonaj@temf.tu-darmstadt.de
[‡] weiland@temf.tu-darmstadt.de

I. INTRODUCTION

Memory consumption and CPU time represent the main limitations for large-scale electromagnetic field computations. This is especially the case for accelerator physics simulations involving self-consistent charged particle models based on the so-called *Particle-In-Cell* (PIC) method [1]. Simulations of this type are an indispensable tool for the design and optimization of particle accelerators since they offer a full insight into the beam dynamics down to the particle level. This is especially important for the simulation of low-energy sections of an accelerator, where space charge forces heavily influence the beam but also for, e.g., dark current or electron cloud simulations. Apart from the solution of Maxwell's equations on a discrete grid space, PIC simulations also include the self-consistent solution of the equations of motion. Thus, they provide a full description of the accelerator structure including space-charge and wakefield effects [2].

In this article we address the important problem of numerical efficiency of such beam dynamics simulations using the Finite Integration Technique (FIT). The FIT has been successfully applied for the simulation of a wide range of electromagnetic problems in accelerator physics [3, 4]. We propose an extension of this method including dynamic mesh refinement in order to locally adjust the spatial grid resolution according to the dynamics of particles and fields. This leads to considerable savings in the overall number of computational degrees of freedom and, thus, reduces the computational burden in PIC simulations.

The article is organized as follows. After describing the governing equations in Sec. II, a brief review of the FIT on static grids is given in Sec. III, which also serves for introducing the notation. Sec. IV describes the dynamic mesh refinement procedures and Sec. V addresses specific issues of charged particle simulations on dynamically refined meshes. Sec. VI contains two applications. First, an example with known analytical solution is considered for investigating accuracy and efficiency of the proposed method. After, results of a detailed design study of the PITZ photo injector using self-consistent PIC simulations are presented. The achievements are summarized in Sec. VII.

II. FORMULATION OF THE PHYSICAL PROBLEM

The electromagnetic part of the physical problem considered is described by Maxwell's equations. Their integral form reads

$$\int_{\partial A} \vec{H} \cdot d\vec{s} = \int_A \left(\frac{\partial}{\partial t} \vec{D} + \vec{J} \right) \cdot d\vec{A}, \quad (1)$$

$$\int_{\partial A} \vec{E} \cdot d\vec{s} = - \int_A \frac{\partial}{\partial t} \vec{B} \cdot d\vec{A}, \quad (2)$$

$$\int_{\partial V} \vec{D} \cdot d\vec{A} = \int_V \rho \, dV, \quad (3)$$

$$\int_{\partial V} \vec{B} \cdot d\vec{A} = 0, \quad (4)$$

where A and V denote arbitrary surfaces and volumes. The magnetic field strength is indicated by \vec{H} , \vec{B} denotes the magnetic flux density, \vec{E} the electric field strength, \vec{D} the dielectric flux density, and \vec{J} the electric current density. The electric and magnetic quantities are related according to the constitutive equations

$$\vec{D} = \epsilon \vec{E}, \quad (5)$$

$$\vec{B} = \mu \vec{H}. \quad (6)$$

For the linear, isotropic, nondispersive materials considered here the permittivity ϵ and the permeability μ are material dependent constants. The conservation of charge follows from Ampère's law (1) and Gauss' law (3) in the form of the continuity equation

$$\frac{d}{dt} \int_V \rho \, dV + \int_{\partial V} \vec{J} \cdot d\vec{A} = 0. \quad (7)$$

It reflects that a temporal change of the total charge, $Q = \int_V \rho \, dV$, contained in a volume is caused only by a flow of electric current into or out of the volume.

The link between Maxwell's equations and the motion of charged particles is established by the Lorentz force

$$\vec{F} = q \left(\vec{E} + \frac{\vec{u}'}{\gamma} \times \vec{B} \right), \quad (8)$$

on the one hand and Newton's law

$$\vec{F} = \frac{d}{dt} \vec{p}, \quad (9)$$

on the other hand. Above, q is the charge of the particle, γ is the relativistic factor and $\vec{u}' = \gamma \vec{v}$, with \vec{v} the velocity of the particle. The mechanical momentum is denoted by \vec{p} .

The equations of motion, thus, read

$$\frac{d}{dt}\vec{u} = \frac{\vec{u}'}{\gamma}, \quad (10)$$

$$\frac{d}{dt}\vec{u}' = \frac{q}{m_0} \left(\vec{E} + \frac{\vec{u}'}{\gamma} \times \vec{B} \right), \quad (11)$$

where \vec{u} is the position vector and m_0 the particle mass at rest.

III. THE FINITE INTEGRATION FRAMEWORK

For introducing the notation as well as for completeness this section comprises a short review of the Finite Integration Technique. For the spatial discretization of Maxwell's equations, it utilizes a staggered, dual orthogonal grid doublet $(\mathcal{G}, \tilde{\mathcal{G}})$ consisting of N_p primary nodes, which covers the domain of interest Ω . The staggered grid arrangement is depicted in Fig. 1. Throughout this article, we employ the FIT on Cartesian grids in three-dimensional space. The following discrete integral state variables are introduced

$$\begin{aligned} \bar{e} &:= \int_c \vec{E} \cdot d\vec{s}, & \bar{h} &:= \int_{\tilde{c}} \vec{H} \cdot d\vec{s}, \\ \hat{b} &:= \int_A \vec{B} \cdot d\vec{A}, & \hat{d} &:= \int_{\tilde{A}} \vec{D} \cdot d\vec{A}, \\ \hat{j} &:= \int_{\tilde{A}} \vec{J} \cdot d\vec{A}, & q &:= \int_{\tilde{V}} \rho dV, \end{aligned} \quad (12)$$

where c and A belong to the set of edges and faces of the primary grid (black), and \tilde{c} , \tilde{A} and \tilde{V} belong to the set of edges, faces and volumes of its dual (gray). The quantities \bar{e} and \bar{h} represent grid voltages, whereas \hat{b} , \hat{d} and \hat{j} are field fluxes on the faces of the grid.

Summing up the voltages \bar{e} and \bar{h} along the four edges enclosing one face yields a discrete but exact representation of Ampère's and Faraday's law, (1) and (2), in the form

$$\sum_{j=1}^4 \pm \bar{h}_j = \frac{d}{dt} \hat{d} + \hat{j}, \quad (13)$$

$$\sum_{j=1}^4 \pm \bar{e}_j = -\frac{d}{dt} \hat{b}, \quad (14)$$

for every face of the computational grid. The orientation of the involved voltages \bar{e}_j , \bar{h}_j with respect to the orientation of the loop integral in (1) and (2) determines the summation signs (see Fig. 1).

The discrete Gauss' laws are obtained in a similar way by summing up the electric and magnetic flux variables $\widehat{\mathbf{d}}$ and $\widehat{\mathbf{b}}$ defined on all faces of a cell. Fluxes pointing out of the cell are counted positive, incoming fluxes negative. This yields the algebraic set of equations

$$\sum_{j=1}^6 \pm \widehat{d}_j = q, \quad (15)$$

$$\sum_{j=1}^6 \pm \widehat{b}_j = 0, \quad (16)$$

for every cell of \mathcal{G} and $\widetilde{\mathcal{G}}$ corresponding to the Gauss' law for electric and magnetic charges, respectively.

The constitutive equations (5) and (6) translate to

$$\widehat{\mathbf{d}} = M_\epsilon \widehat{\mathbf{e}}, \quad (17)$$

$$\widehat{\mathbf{b}} = M_\mu \widehat{\mathbf{h}}, \quad (18)$$

where M_ϵ and M_μ provide an appropriate mapping of grid voltages into fluxes [3].

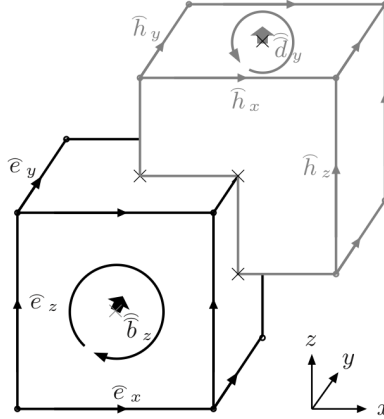


FIG. 1. Staggered grid doublet in FIT. The primary grid and its associated quantities are depicted in black, the dual grid in gray.

Collecting the N_p voltages and fluxes in the vectors $\widehat{\mathbf{e}}$, $\widehat{\mathbf{h}}$, $\widehat{\mathbf{b}}$, $\widehat{\mathbf{d}}$ and $\widehat{\mathbf{j}}$ allows for stating (13)-(16) for the complete computational domain in the compact form

$$\mathbf{C} \widehat{\mathbf{e}} = -\frac{d}{dt} \widehat{\mathbf{b}}, \quad (19)$$

$$\widetilde{\mathbf{C}} \widehat{\mathbf{h}} = \frac{d}{dt} \widehat{\mathbf{d}} + \widehat{\mathbf{j}}, \quad (20)$$

$$\widetilde{\mathbf{S}} \widehat{\mathbf{d}} = \mathbf{q}, \quad (21)$$

$$\mathbf{S} \widehat{\mathbf{b}} = \mathbf{0}. \quad (22)$$

The summation signs are gathered together in the matrices \mathbf{C} , $\tilde{\mathbf{C}}$ and \mathbf{S} , $\tilde{\mathbf{S}}$. These matrices are, hence, purely topological. They represent a discrete curl and divergence operator of the FIT. It can be shown that these operators maintain the properties of their counterparts in continuum [5] in the sense that

$$\begin{aligned}\mathbf{S}\mathbf{C} &= 0, & \tilde{\mathbf{S}}\tilde{\mathbf{C}} &= 0, \\ \mathbf{C}\tilde{\mathbf{S}}^T &= 0, & \tilde{\mathbf{C}}\mathbf{S}^T &= 0.\end{aligned}$$

This allows, e.g., for the derivation of a discrete continuity equation [cf. Eqn. (7)] in the form

$$\frac{d}{dt}\mathbf{q} + \tilde{\mathbf{S}}\hat{\mathbf{j}} = \mathbf{0}. \quad (23)$$

Eqns. (19)-(22) are called Maxwell grid equations (MGE). Typically, the leap-frog scheme is applied for their integration in time. Alternatively, one may apply the longitudinal-transverse split operator scheme introduced in [6, 7] for the time integration, which offers better numerical dispersion properties. The latter approach is referred to as LT-FIT standing for Longitudinal-Transverse-FIT.

IV. DYNAMIC MESH REFINEMENT

We will restrict the discussion to conformal mesh refinements, which maintain the conformity and duality of the Cartesian grid doublet. A refined mesh is obtained by a sequence of bisections applied to a given mesh cell. The number of consecutive bisections of a cell is referred to as its refinement level L (see Fig. 2).

When mesh refinement is applied the discrete quantities assigned to the primary and the dual grid need to be recomputed according to the modified mesh. In Fig. 3 the refinement of a primary grid cell and the subsequent arrangement of electric grid voltages is illustrated in a two-dimensional cut view. The preservation of the duality of the staggered grids requires adding new nodes to the dual grid, as well as shifting existing nodes. This is shown in Fig. 4. In order to obtain a value for the new or shifted voltages an interpolation procedure has to be carried out. Furthermore, it has to be distinguished between the interpolation of voltages oriented in parallel to the refinement [e.g. $\tilde{e}'_x(2')$ in Fig. 3(b)] and those oriented perpendicularly [e.g. $\tilde{e}'_z(2)$ and $\tilde{e}'_z(2')$ in Fig. 3(c)]. In the following, two interpolation procedures, linear and high order spline interpolation, will be discussed.

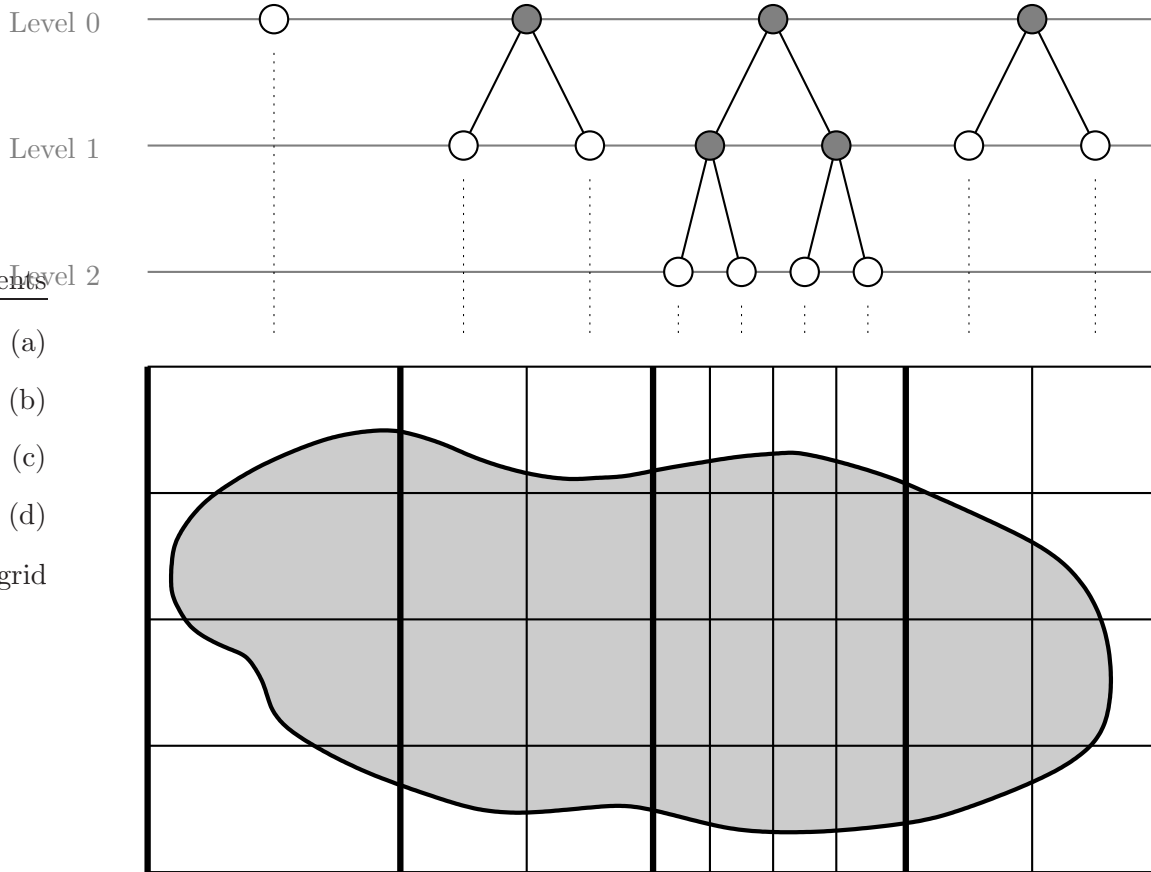


FIG. 2. Representation of the mesh refinement using consecutive bisections and the refinement levels. Non-refined grid cells, such as the cells on the left end have refinement level zero. Each bisection increases the refinement level by one, which can be represented by means of a binary tree structure. The grid step size at level L reduces as $1/2^L$.

A. Linear Interpolation of Grid Voltages

The application of a linear interpolation for the determination of new or shifted voltages is straightforward. The interpolation procedure described below refers to the refinement scenario shown in Fig. 3 and 4. The lengths of the primary and dual grid edges [cf. (12)] are denoted by $|c|$ and $|\tilde{c}|$, respectively. Discrete field quantities associated with a specific node i or \tilde{i} are denoted as, e.g., $c(i)$. Primed quantities are either new or they have to be recomputed during the adaptation procedure.

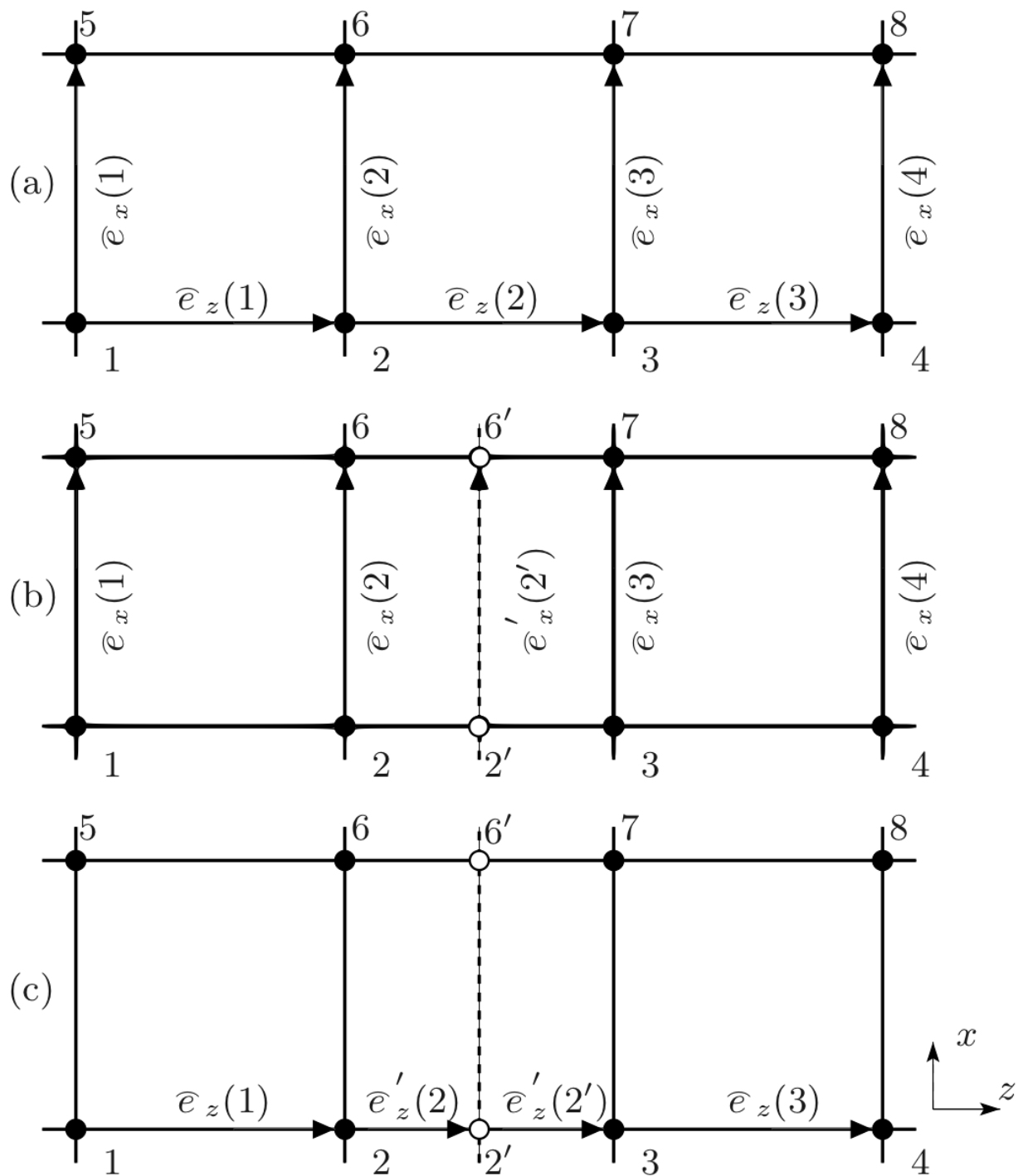


FIG. 3. The refinement of the primary grid and the assignment of electric grid voltages to the refined edges is depicted in the $x - z$ plane. In (a) the initial situation is shown. In (b) and (c) the middle cell was refined, introducing an additional grid line (dashed). Thus, two nodes $2'$ and $6'$ (circles) are inserted. All voltages that are new or require an update of their value are marked with a prime. In (b) the position of the new electric grid voltage $\bar{e}'_x(2')$ is shown. The voltage $\bar{e}_z(2)$, oriented along the z -coordinate, has to be split into the two voltages $\bar{e}'_z(2)$ and $\bar{e}'_z(2')$ as shown in (c).

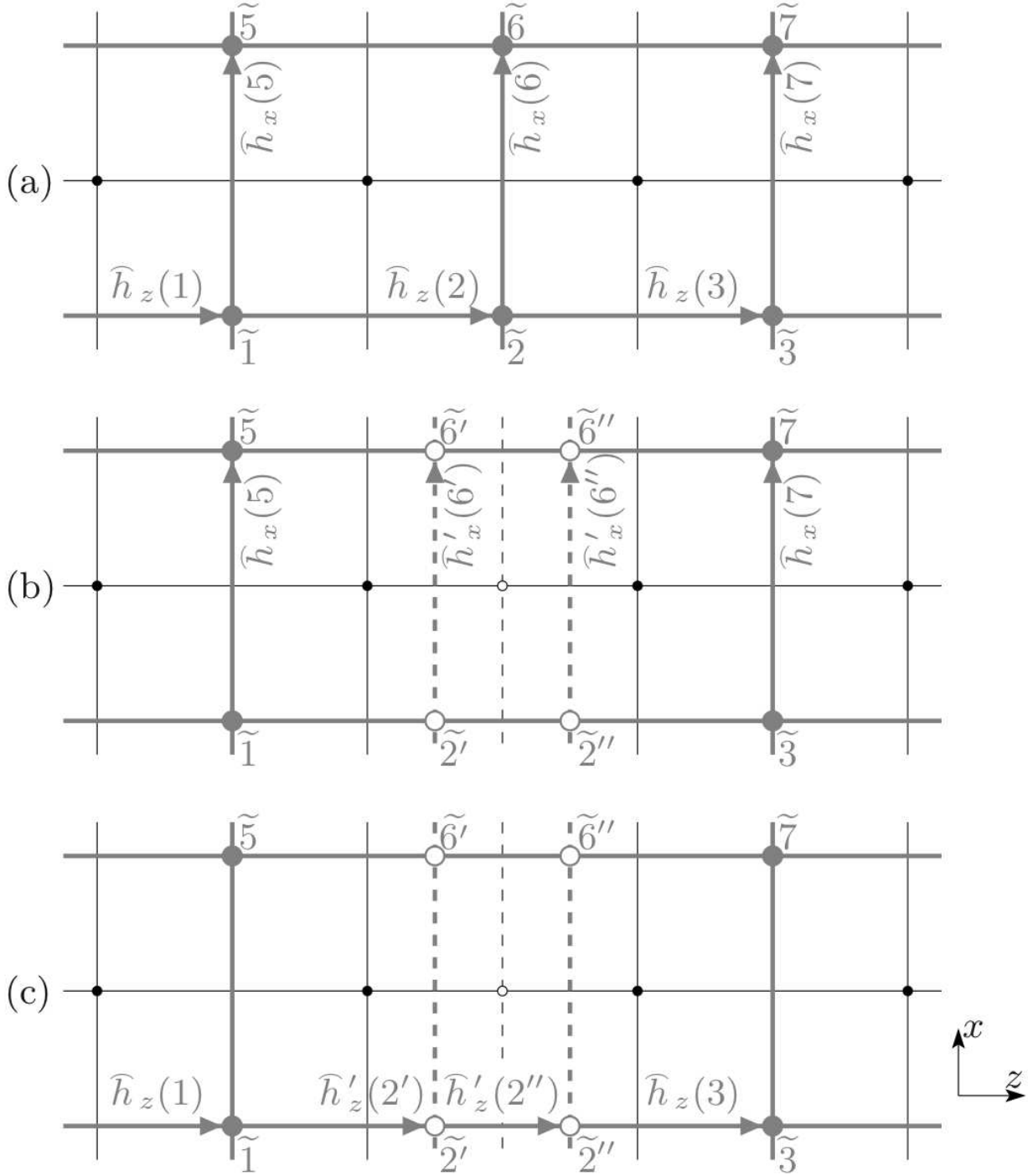


FIG. 4. The refinement of the dual grid (gray), imposed by the refined primary grid (thin black lines) is depicted. The initial situation is shown in (a). In order to preserve the duality of the two grids the dual nodes $\tilde{2}$ and $\tilde{6}$ have to be shifted. Their new position is indicated by $\tilde{2}'$ and $\tilde{6}'$ in (b) and (c). In addition, the two new nodes $\tilde{2}''$ and $\tilde{6}''$ have to be inserted. In (b) the assignment of x -oriented magnetic voltages is shown and in (c) the assignment of z -oriented voltages.

a. Refinement The values of new electric grid voltages oriented parallel to the refinement [e.g. $\bar{e}'_x(2')$] are determined by

$$\bar{e}'_x(2') = \frac{\bar{e}_x(2) + \bar{e}_x(3)}{2}. \quad (24)$$

The splitting of voltages oriented perpendicularly to the refinement [e.g. $\bar{e}_z(2)$] is constrained by the condition

$$\bar{e}'_z(2) + \bar{e}'_z(2') \stackrel{!}{=} \bar{e}_z(2). \quad (25)$$

This condition imposes the conservation of the total voltage between the nodes 2 and 3. A detailed sketch of this refinement is shown in Fig. 5. In order to assign values to the refined voltages $\bar{e}'_z(2)$ and $\bar{e}'_z(2')$ the voltage gradient, i.e., the average electric field, along the axis is approximated by a central difference using the neighboring voltages $\bar{e}_z(1)$ and $\bar{e}_z(3)$. The voltages assigned to the refined edges read

$$\bar{e}'_z(2) = |c'(2)| \cdot \left(e_z(2) - \frac{|c'(2)|}{2} \cdot \frac{\Delta e_z(3, 1)}{\Delta z(\tilde{3}, \tilde{1})} \right), \quad (26)$$

$$\bar{e}'_z(2') = |c'(2')| \cdot \left(e_z(2) + \frac{|c'(2')|}{2} \cdot \frac{\Delta e_z(3, 1)}{\Delta z(\tilde{3}, \tilde{1})} \right), \quad (27)$$

where the sampled electric field variables $e_z(i)$ are introduced as

$$e_z(i) := \frac{\bar{e}_z(i)}{|c(i)|}, \quad (28)$$

the z -coordinate of the node i is denoted by $z(i)$, and the Δ -notation denotes a difference of the respective quantity, e.g., $\Delta z(\tilde{3}, \tilde{1}) = z(\tilde{3}) - z(\tilde{1})$. Since cells are always divided into halves, $|c'(2)|$ equals $|c'(2')|$ and the condition (25) is fulfilled.

The interpolation of the magnetic voltages is more cumbersome. Besides the insertion of new dual grid nodes, also existing nodes have to be shifted in position in order to preserve the duality of the staggered grids. Shifting a node, however, implies a modification of the grid voltages along the associated edges.

The interpolation of magnetic voltages oriented in parallel to the refinement is illustrated in Fig. 4(b). The voltages $\bar{h}'_x(\tilde{6}')$ and $\bar{h}'_x(\tilde{6}'')$ are given by

$$\bar{h}'_x(\tilde{6}') = \bar{h}_x(\tilde{6}) - \Delta z(\tilde{6}, \tilde{6}') \cdot \frac{\Delta \bar{h}_x(\tilde{7}, \tilde{5})}{\Delta z(\tilde{7}, \tilde{5})}, \quad (29)$$

$$\bar{h}'_x(\tilde{6}'') = \bar{h}_x(\tilde{6}) + \Delta z(\tilde{6}'', \tilde{6}) \cdot \frac{\Delta \bar{h}_x(\tilde{7}, \tilde{5})}{\Delta z(\tilde{7}, \tilde{5})}. \quad (30)$$

Similarly to the splitting of electric voltages, the splitting of magnetic voltages, oriented perpendicularly to the refinement, is constrained by the conservation of the total voltage. However, for a complete description of the refinement algorithm, the bisection of at least two neighboring cells has to be considered. This is illustrated in Fig. 6. For this case, the conservation condition for the total voltage between the nodes $\tilde{1}$ and $\tilde{4}$ can be expressed as

$$\bar{h}'_z(\tilde{2}') + \bar{h}'_z(\tilde{2}'') + \bar{h}'_z(\tilde{3}') + \bar{h}'_z(\tilde{3}'') + \bar{h}'_z(\tilde{4}) \stackrel{!}{=} \bar{h}_z(\tilde{2}) + \bar{h}_z(\tilde{3}) + \bar{h}_z(\tilde{4}). \quad (31)$$

The refined magnetic voltages read

$$\begin{aligned} \bar{h}'_z(\tilde{2}') &= |\tilde{c}'(\tilde{2}')| \cdot \left[h_z(\tilde{2}) - \left(z(2) - \frac{z(\tilde{1}) + z(\tilde{2}')}{2} \right) \right. \\ &\quad \left. \cdot \frac{\Delta h_z(\tilde{4}, \tilde{2})}{\Delta z(4, 2)} \right], \end{aligned} \quad (32)$$

$$\bar{h}'_z(\tilde{2}'') = \Delta z(\tilde{2}, \tilde{2}') \cdot h_z(\tilde{2}) + \Delta z(\tilde{2}'', \tilde{2}) \cdot h_z(\tilde{3}), \quad (33)$$

$$\bar{h}'_z(\tilde{3}') = |\tilde{c}'(\tilde{3}')| \cdot h_z(\tilde{3}), \quad (34)$$

$$\bar{h}'_z(\tilde{3}'') = \Delta z(\tilde{3}, \tilde{3}') \cdot h_z(\tilde{3}) + \Delta z(\tilde{3}'', \tilde{3}) \cdot h_z(\tilde{4}), \quad (35)$$

$$\begin{aligned} \bar{h}'_z(\tilde{4}) &= |\tilde{c}'(\tilde{4})| \cdot \left[h_z(\tilde{4}) + \left(\frac{z(\tilde{3}'') + z(\tilde{4})}{2} - z(4) \right) \right. \\ &\quad \left. \cdot \frac{\Delta h_z(\tilde{4}, \tilde{2})}{\Delta z(4, 2)} \right], \end{aligned} \quad (36)$$

with the sampled magnetic field $h_z(\tilde{i})$ defined as

$$h_z(\tilde{i}) := \frac{\bar{h}_z(\tilde{i})}{|\tilde{c}'(\tilde{i})|}. \quad (37)$$

Since the following equations hold true

$$z(2) - \frac{z(\tilde{1}) + z(\tilde{2}')}{2} = \frac{z(\tilde{3}'') + z(\tilde{4})}{2} - z(4), \quad (38)$$

and

$$|\tilde{c}(\tilde{2})| = |\tilde{c}'(\tilde{2}')| + \Delta z(\tilde{2}, \tilde{2}'), \quad (39)$$

$$|\tilde{c}(\tilde{3})| = \Delta z(\tilde{2}'', \tilde{2}) + |\tilde{c}'(\tilde{3}')| + \Delta z(\tilde{3}, \tilde{3}'), \quad (40)$$

$$|\tilde{c}(\tilde{4})| = \Delta z(\tilde{3}'', \tilde{3}) + |\tilde{c}'(\tilde{4})|, \quad (41)$$

the Eqns. (32)-(36) fulfill the condition (31).

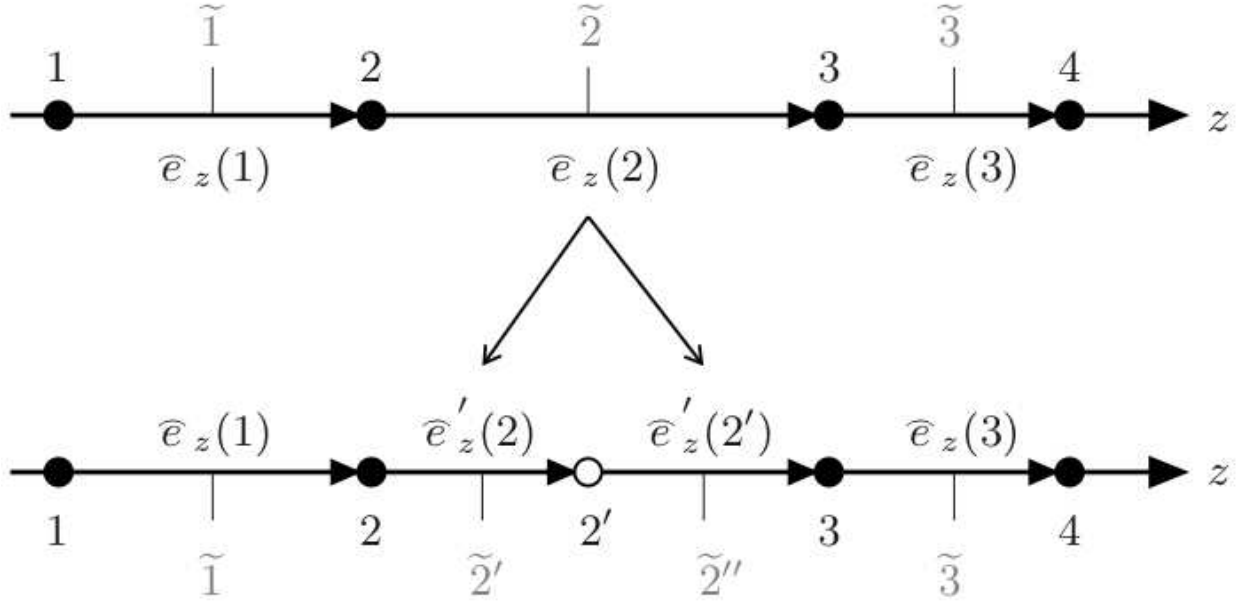


FIG. 5. Interpolation of electric grid voltages oriented perpendicularly to the refinement. The coarse grid voltage $\bar{e}_z(2)$ is split into the two voltages $\bar{e}'_z(2)$ and $\bar{e}'_z(2')$ such that the total voltage in between the nodes 2 and 3 is preserved [cf. Eqn. (25)]. In order to assign values to $\bar{e}'_z(2)$ and $\bar{e}'_z(2')$ the voltage gradient along the axis is evaluated using $\bar{e}_z(1)$ and $\bar{e}_z(3)$ [cf. Eqns. (26), (27)].

The Eqns. (24), (26), (27), (29), (30), and (32)-(36) define the rules for performing linear interpolations of the state variables $\bar{\mathbf{e}}$ and $\bar{\mathbf{h}}$. They enable consistent grid refinement based on cell bisection within the FIT framework.

b. Coarsening In the following, the rules for performing grid coarsening are given. We refer again to the Figs. 3 and 4 and assume the removal of the nodes $2'$ and $6'$ and the associated dual nodes. Alongside with the removal of the primary nodes $2'$ and $6'$ and the connecting edge, the electric grid voltage $\bar{e}'_z(2')$ is eliminated from the vector of electric voltages. No further modification is required for all electric voltages oriented in parallel to the refinement. The constraint (25) defines the rule for merging electric voltages oriented perpendicularly to the refinement

$$\bar{e}_z(2) = \bar{e}'_z(2) + \bar{e}'_z(2'). \quad (42)$$

For the determination of the magnetic coarse grid voltage $\bar{h}_x(\bar{6})$, oriented parallel to the refinement, a linear interpolation of the neighboring voltages allocated on the refined grid

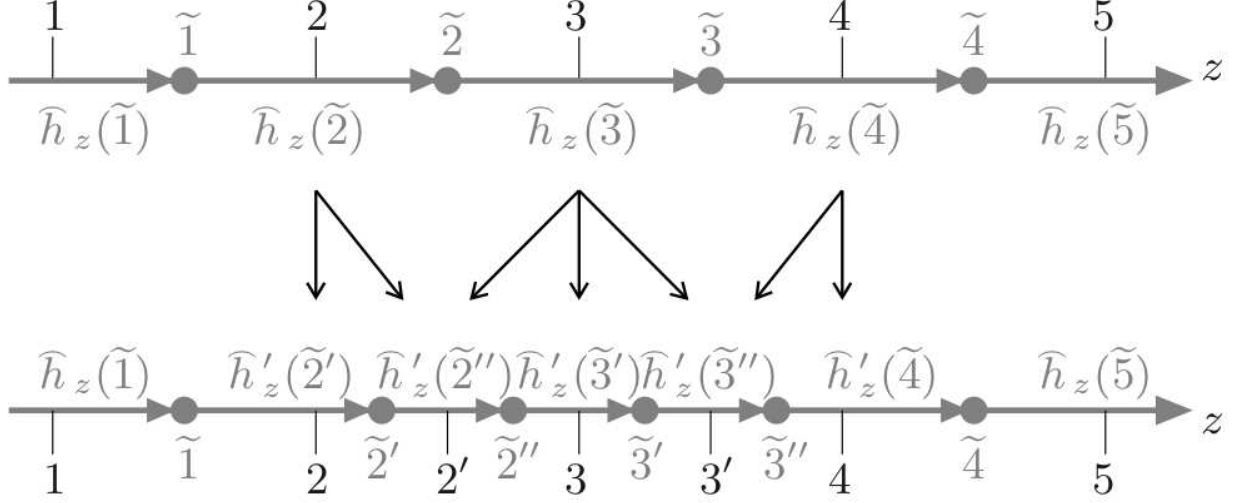


FIG. 6. Interpolation of magnetic grid voltages oriented perpendicularly to the refinement. The voltages $\hat{h}_z(\tilde{2})$, $\hat{h}_z(\tilde{3})$ and $\hat{h}_z(\tilde{4})$, assigned to coarse grid edges, are split and distributed such that the total magnetic voltage in between the nodes $\tilde{2}$ and $\tilde{4}$ is preserved [cf. Eqn. (31)]. The voltages on the refined grid are determined according to the [cf. Eqns. (32)-(36)].

is performed

$$\hat{h}_x(\tilde{6}) = \frac{\hat{h}'_x(\tilde{6}') + \hat{h}'_x(\tilde{6}'')}{2}. \quad (43)$$

The magnetic coarse grid voltages, oriented perpendicularly to the refinement, are obtained by the summation of fractional voltages given on the fine grid (see Fig. 6). The merging of the fine grid magnetic voltages has to obey the constraint (31). The coarse grid voltages are given by

$$\hat{h}_z(\tilde{2}) = \hat{h}'_z(\tilde{2}') + \Delta z(\tilde{2}, \tilde{2}') \cdot h'_z(\tilde{2}''), \quad (44)$$

$$\begin{aligned} \hat{h}_z(\tilde{3}) &= \Delta z(\tilde{2}'', \tilde{2}) \cdot h'_z(\tilde{2}'') \\ &\quad + \hat{h}'_z(\tilde{3}') + \Delta z(\tilde{3}, \tilde{3}') \cdot h'_z(\tilde{3}''), \end{aligned} \quad (45)$$

$$\hat{h}_z(\tilde{4}) = \Delta z(\tilde{3}'', \tilde{3}) h'_z(\tilde{3}'') + \hat{h}'_z(\tilde{4}). \quad (46)$$

Since the following holds true

$$|\tilde{c}(\tilde{2}'')| = \Delta z(\tilde{2}, \tilde{2}') + \Delta z(\tilde{2}'', \tilde{2}), \quad (47)$$

$$|\tilde{c}(\tilde{3}'')| = \Delta z(\tilde{3}, \tilde{3}') + \Delta z(\tilde{3}'', \tilde{3}), \quad (48)$$

the condition (31) is fulfilled also for the case of grid coarsening.

Eqns. (??)-(46) describe the required modifications of the FIT field quantities during the coarsening process of the computational grid. In combination with the refinement rules given above, they provide a consistent framework for performing time-adaptive conformal grid refinement within the FIT. Refinement schemes other than by cell bisecting are generally possible. However, these are associated with a larger complexity in mesh administration and will not be considered in this work.

B. Spline Interpolation

A linear interpolation of the discrete field quantities is easy to implement and fast in code execution. The interpolated quantities are second order accurate, which is in agreement with the theoretical order of accuracy of the FIT. However, applying higher order interpolating functions may be beneficial for obtaining a smoother representation of high-frequency fields on the refined mesh.

Polynomials offer a possibility for performing higher order interpolations. However, polynomials of high degrees tend to exhibit an oscillatory behavior and possibly large overshoots, known as Runge’s phenomenon [8]. Commonly, spline functions are employed in order to avoid this behavior.

A spline S is a piecewise defined polynomial function of order P which is $P - 1$ times continuously differentiable, i.e., $S \in \mathcal{C}^{P-1}$ [9]. The construction rules determine the specific type of spline. If the spline S is demanded to pass exactly through the given data points, and to be twice continuously differentiable (i.e. $S \in \mathcal{C}^2$) with the second derivative equal to zero on every interval boundary, the so-called natural cubic spline (C-spline) is obtained. For its determination, a tridiagonal system of equations has to be solved. During a time-domain simulation adopting time-adaptive grid refinement, hundreds to thousands of grid adaptations are performed, each involving thousands of cells. Thus, the solution of a system of equations is computationally very expensive. In addition, the natural cubic spline may still exhibit overshoots (see Fig. 7).

In order to further mitigate Runge’s phenomenon, the conditions on the continuous differentiability of the spline have to be reduced. A spline S of order P which is at most $P - 2$ times continuously differentiable is called a broken spline or subspline [9]. The Akima spline is a cubic subspline which is an element of the functional space \mathcal{C}^1 [10]. Cubic (sub-)splines

can conveniently be characterized by the triple of values $[x(i), f(i), s(i)]$ for each data point i , where $x(i)$ is the coordinate of the data point, $f(i)$ its value, and $s(i)$ its slope. Imposing the conditions

$$\begin{aligned} S[x(i-1)] &= f(i-1), & S[x(i)] &= f(i), \\ S'[x(i-1)] &= s(i-1), & S'[x(i)] &= s(i), \end{aligned}$$

at every interval boundary, uniquely describes the broken cubic spline function

$$S(x) = a_0 + a_1[x - x(i-1)] + a_2[x - x(i-1)]^2 + a_3[x - x(i-1)]^3, \quad (49)$$

with the coefficients

$$\begin{aligned} a_0 &= f(i-1), \\ a_1 &= s(i-1), \\ a_2 &= \frac{3}{(\Delta x)^2} \Delta f(i, i-1) - \frac{1}{\Delta x} [s(i) + 2s(i-1)], \\ a_3 &= \frac{2}{(\Delta x)^3} \Delta f(i, i-1) + \frac{1}{(\Delta x)^2} \Delta s(i, i-1). \end{aligned}$$

However, the slopes $s(i)$ are, in general, unknown. The Akima procedure makes use of a local heuristic method for the estimation of the slopes. It involves the data point i and two neighboring points on each side. First, the piecewise gradients g , given by

$$g(j) := \frac{f(j+1) - f(j)}{x(j+1) - x(j)}, \quad \text{with } j = i-2, i-1, i, i+1,$$

are evaluated. These are weighted with the factors w

$$\begin{aligned} w(i-1) &:= |g(i+1) - g(i)|, \\ w(i) &:= |g(i-1) - g(i-2)|, \end{aligned}$$

yielding the estimated slope at data point i

$$s(i) := \frac{w(i-1)g(i-1) + w(i)g(i)}{w(i-1) + w(i)}. \quad (50)$$

The fundamental idea of the heuristic can be summarized as: the larger the difference between the two gradients on one side of point i , the larger is the weighting factor applied to the gradient on the other side of this point. This is intended to minimize overshooting and oscillatory behavior. Note that, Akima's heuristic is closely related to the idea of slope

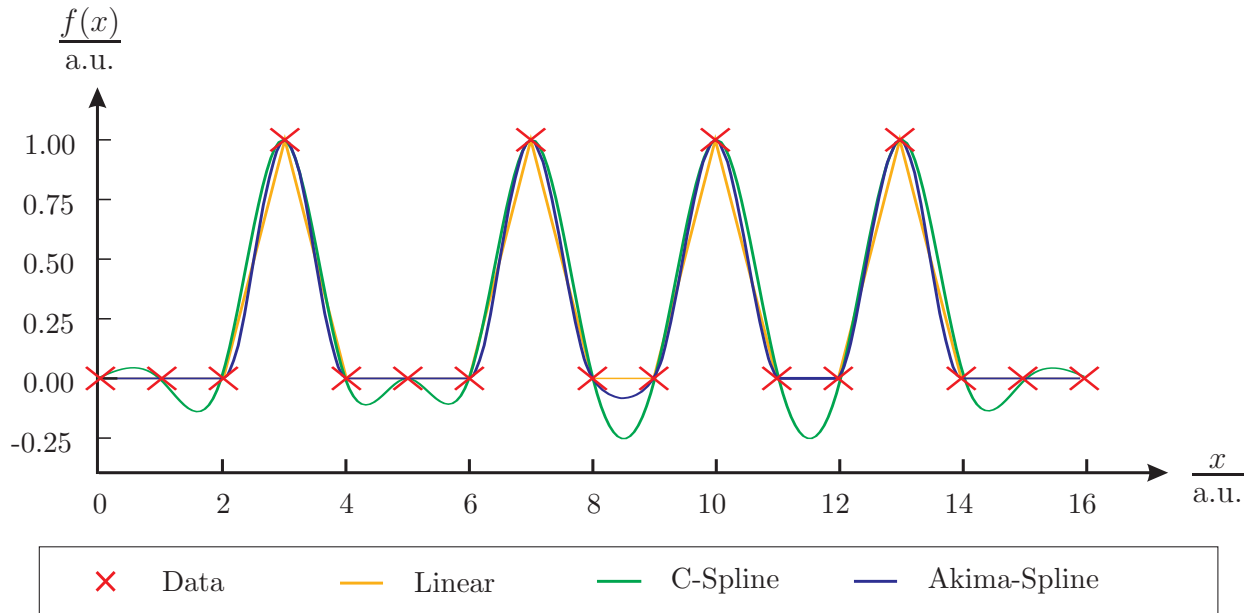


FIG. 7. Comparison of spline interpolations. The given data points are interpolated using linear interpolation, a natural cubic spline (C-spline) and an Akima spline. The C-spline exhibits an oscillatory behavior and strong overshooting. Up to the data point 10, Akima’s original slope estimation was employed [cf. Eqn. (50)]. From this point on the minmod slope limiter [cf. Eqn. (51)] was applied, which effectively avoids overshooting.

limiters. These are commonly used in Finite Volume methods for reconstructing a piecewise continuous solution on the grid (cf. [11]). Using, e.g., the minmod limiter the estimated slope reads

$$\begin{aligned}
 s(i) &:= \text{minmod}[g(i), g(i+1)] \\
 &= \begin{cases} g(i), & \{\forall i \mid |g(i)| < |g(i+1)|, g(i)g(i+1) > 0\}, \\ g(i+1), & \{\forall i \mid |g(i)| > |g(i+1)|, g(i)g(i+1) > 0\}, \\ 0, & \{\forall i \mid g(i)g(i+1) \leq 0\}. \end{cases} \quad (51)
 \end{aligned}$$

Out of its two arguments, the minmod operator chooses the smaller one if they are equally signed and zero otherwise. An overview of slope limiting techniques is found in [12].

In Fig. 7 the interpolation of a set of data points using linear interpolation, the C-spline and the Akima spline is illustrated. The C-spline shows an oscillatory behavior and strong overshooting. For the determination of the Akima spline up to data point 10, the slope was

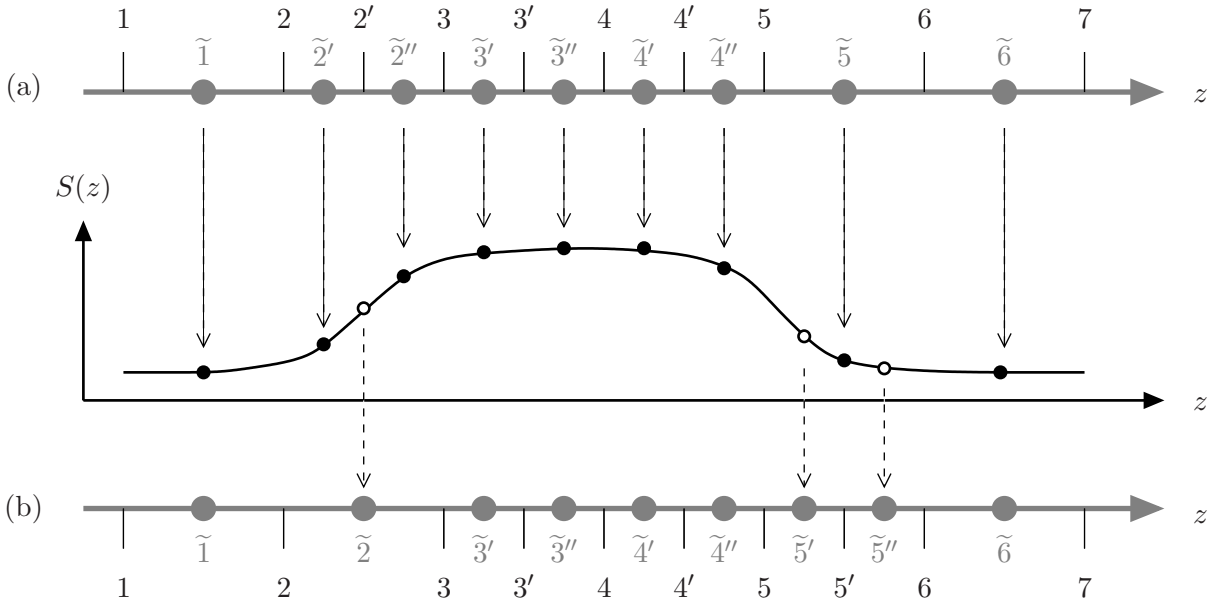


FIG. 8. Setup and evaluation of the interpolating spline. An exemplary arrangement of grid nodes along the z -coordinate is shown in (a) and (b). In (b) the refined area of the grid has moved by a distance of one grid cell into the z -direction. Hence, the grid has to be coarsened around node 2 and refined around node 5. The interpolating spline is set up, using the position of the nodes and field data in the refined area and some neighboring cells (black dots). An evaluation of the spline function at the position of new or shifted nodes (circles), yields the interpolated field values.

calculated using Akima's slope definition (50). For the points 11 to 16 the minmod limiter was applied, which effectively avoids any overshooting.

The actual spline interpolation procedure of the discrete field quantities is illustrated in Fig. 8. In (a) and (b) the primary and dual grid nodes along the z -coordinate are indicated in black and gray. In (b) the refined area has moved by a distance of one grid cell into the z -direction. Therefore, the grid topology around the cells 2 (coarsening) and 5 (refinement) has to be modified. The spline is set up using the position of the grid nodes and the allocated field data in the refined area and some neighboring cells. An evaluation of the spline function at the position of new or shifted nodes yields the interpolated field values.

The Akima and the slope limited splines are viable choices for performing interpolations within the computational grid. They are formally third order accurate and can be fully constructed from local information. Thus, they do not require the solution of a system of

equations, which makes their implementation very efficient for the purpose of adaptive grid refinement.

V. CHARGED PARTICLE SIMULATIONS ON ADAPTIVE GRIDS

Simulations of the dynamics of charged particles using the FIT are performed routinely and have first been reported in 1988 in [15]. For self-consistent simulations the *particle-in-cell* (PIC) algorithm is applied [16]. It employs *macro particles*, which may adopt any position from the space-continuous domain of interest. Macro particles carry the charge and mass of about $10^{3.5}$ individual particles. Due to (11) the trajectory of a particle in the presence of electromagnetic fields depends only on the ratio of its charge and rest mass, making this a valid simplification.

The PIC algorithm consists of three steps. First, the electromagnetic field at the space-continuous position of each macro particle has to be obtained from the space-discrete FIT quantities. This is done by means of a trilinear interpolation. Next, the equations of motion (10), (11) are integrated using the algorithm described in [17]. Finally, the convective currents are calculated from the position increment of all particles. For this last step we adapted the cloud-in-cell (CIC) approach [18, 19] to work with time-adaptive mesh refinement. The particles are modeled as a uniformly charged volume of finite extent, i.e., a charged cloud.

The extent of the cloud is usually chosen to coincide with the size of the cells. However, if a nonequidistant grid is employed or in the case of adaptive grid refinement, the nonuniform sizes of the cells demand for a modification of the algorithm. There are two modification options: first, a constant size of the particle cloud is chosen independently from the grid cell size or, second, the size of the cloud is adapted in order to match the sizes of the involved cells. Depending on the local degree of grid refinement, the first option can largely increase the number of cells affected by one cloud. Besides the coding efforts coming along with this non-local operation, the deposit of fractional currents to a large number of grid points increases the computational load. Therefore, the second option has been pursued. The adaptation of the cloud in dependence of the grid cell size is illustrated in Fig. 9 for a one-dimensional example.

The modified CIC approach maintains its charge conserving property, meaning that it fulfills the discrete continuity equation (23) in a cell-wise manner.

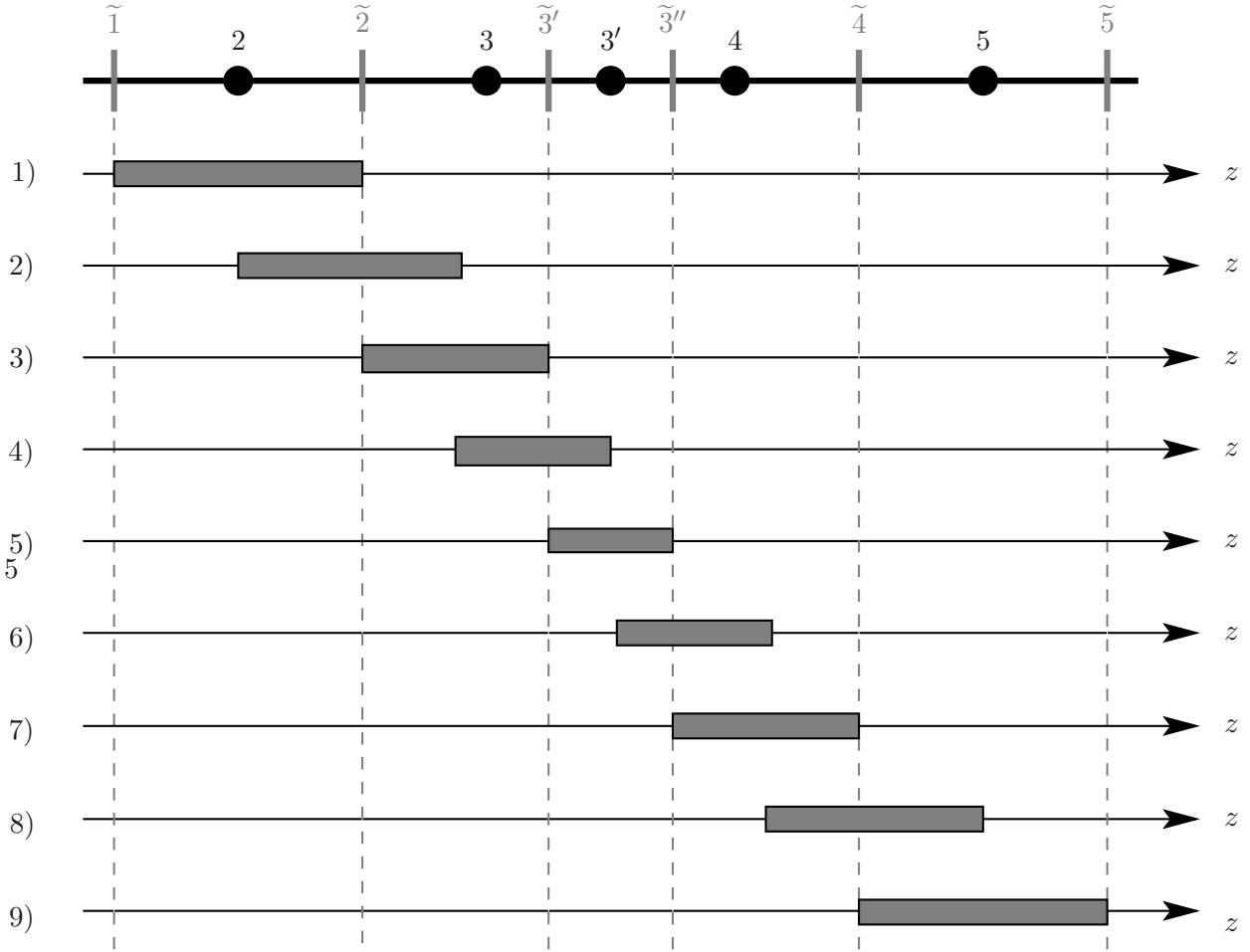


FIG. 9. Illustration of the adaptation of the particle cloud size in one dimension. The size of the particle cloud relates to the extent of the covered cells on the dual grid. If the particle is centered within a dual grid cell (cases 1, 3, 5, 7 and 9) the sizes of the cloud and the dual volume coincide. Otherwise, the cloud has to be adapted asymmetrically around the particle position. For the cases 2 and 4 the charge density within the part of the cloud within the dual volumes $\tilde{2}$ or $\tilde{3}'$ has to be increased as a consequence of the diminished size. Contrarily, for the cases 6 and 8, the charge density of the cloud in the dual volumes $\tilde{3}''$ and $\tilde{4}$ has to be decreased.

VI. APPLICATIONS

In this section, we present results of the application of the dynamic mesh adaptation algorithm introduced above to the simulation of two setups.

A. Bunch drift in a pipe

We consider a hollow, perfectly conducting pipe, which is closed by a perfectly conducting plate at one end. The other end is left open. A bunch of charged particles is emitted from the center of the end plate and travels along the pipe at a constant velocity of $0.9 c_0$, where c_0 is the speed of light in vacuum. The settings of the computational model are specified in Table I. In [20] the analytical solution of this problem for a semi-infinite pipe is given.

TABLE I. Settings of the benchmark example

Pipe length	Pipe radius	RMS bunch radius	RMS bunch length	Particle velocity
120 mm	40 mm	5 mm	3 mm	$0.9 c_0$

In the simulations the axis of the cylinder is aligned with the z -coordinate. In the Figs. 10(a) and 10(c), the analytical solution of the longitudinal electric field along the axis is depicted by a black curve. The solutions obtained with the FIT and the LT-FIT are shown in red and green, respectively. For the results shown in Fig. 10(a), an equidistant grid and the respective maximum time step was applied. In Fig. 10(b) the errors, given by the pointwise Euclidean distance of the analytical and the respective numerical solution, are plotted. The results obtained using dynamic mesh refinement ($L = 3$) in the bunch region are shown in Fig. 10(c) and the errors in Fig. 10(d).

A series of simulations of this test setup using various mesh and mesh refinement settings has been carried out. The results are presented in the Tables II (FIT) and III (LT-FIT). Besides the mesh settings, they list the number of degrees of freedom (DoF) applied as well as the computation time in seconds. The relative L^2 -error and the *total variation* (TV) of the longitudinal electric field along the cylinder axis are given as measures for the quality of the numerical solutions. The relative L^2 -error is computed as

$$\mathcal{E}^{\text{rel}} = \frac{\|\mathbf{E}_z - \mathbf{e}_z\|_2}{\|\mathbf{E}_z\|_2},$$

with $\mathbf{E}_z = (E_z(z(1)), \dots, E_z(z(N_z)))^T$ and E_z the longitudinal component of the analytical solution of the electric field evaluated at the grid point positions $z(i_z)$.

The total variation is a measure for the smoothness of a function [21]. It is defined as

$$TV(E(z)) := \int_{z(1)}^{z(N_z)} |E'(z)| dz. \quad (52)$$

TABLE II. Results of FIT simulations: the upper half shows results for static, equidistant grids, in the lower half the results obtained on time-adaptive grids using Akima splines are displayed.

L	N_x	N_z	$\Delta x / \text{mm}$	$\Delta z_{\min} / \text{mm}$	DoF / 1e6	Time / sec	\mathcal{E}^{rel}	TV
static grid								
0	135	210	0.59	0.57	22.96	2066	0.041	1.00
time-adaptively refined grid								
1	135	105	0.59	0.57	13.00	1225	0.044	1.42
2	135	52	0.59	0.58	9.00	940	0.040	1.93
3	135	27	0.59	0.56	8.50	925	0.041	1.99
4	135	13	0.59	0.58	11.50	1025	0.039	1.55

TABLE III. Results of LT-FIT simulations: the upper half shows results for static, equidistant grids, in the lower half the results obtained on time-adaptive grids using Akima splines are displayed.

L	N_x	N_z	$\Delta x / \text{mm}$	$\Delta z_{\min} / \text{mm}$	DoF / 1e6	Time / sec	\mathcal{E}^{rel}	TV
static grid								
0	135	210	0.59	0.57	22.96	3543	0.038	0.63
time-adaptively refined grid								
1	135	105	0.59	0.57	13.00	2008	0.045	1.39
2	135	52	0.59	0.58	9.00	1443	0.041	1.65
3	135	27	0.59	0.56	8.50	1447	0.040	1.80
4	135	13	0.59	0.58	11.50	1791	0.037	1.40

In [22] it is shown that the TV of a function equals the sum of local minima and maxima, where the values at the integration endpoints count once and all other extrema count twice. The TV is, therefore, a direct measure for oscillations and their amplitudes. For discrete solutions it is computed as

$$TV(\mathbf{e}_z) = \sum_{i_z=1}^{N_z-1} |e_z(i_z + 1) - e_z(i_z)|. \quad (53)$$

The standard FIT is a very well established method for performing PIC simulations. All TV values are, hence, normalized to the value obtained with the FIT on the finest,

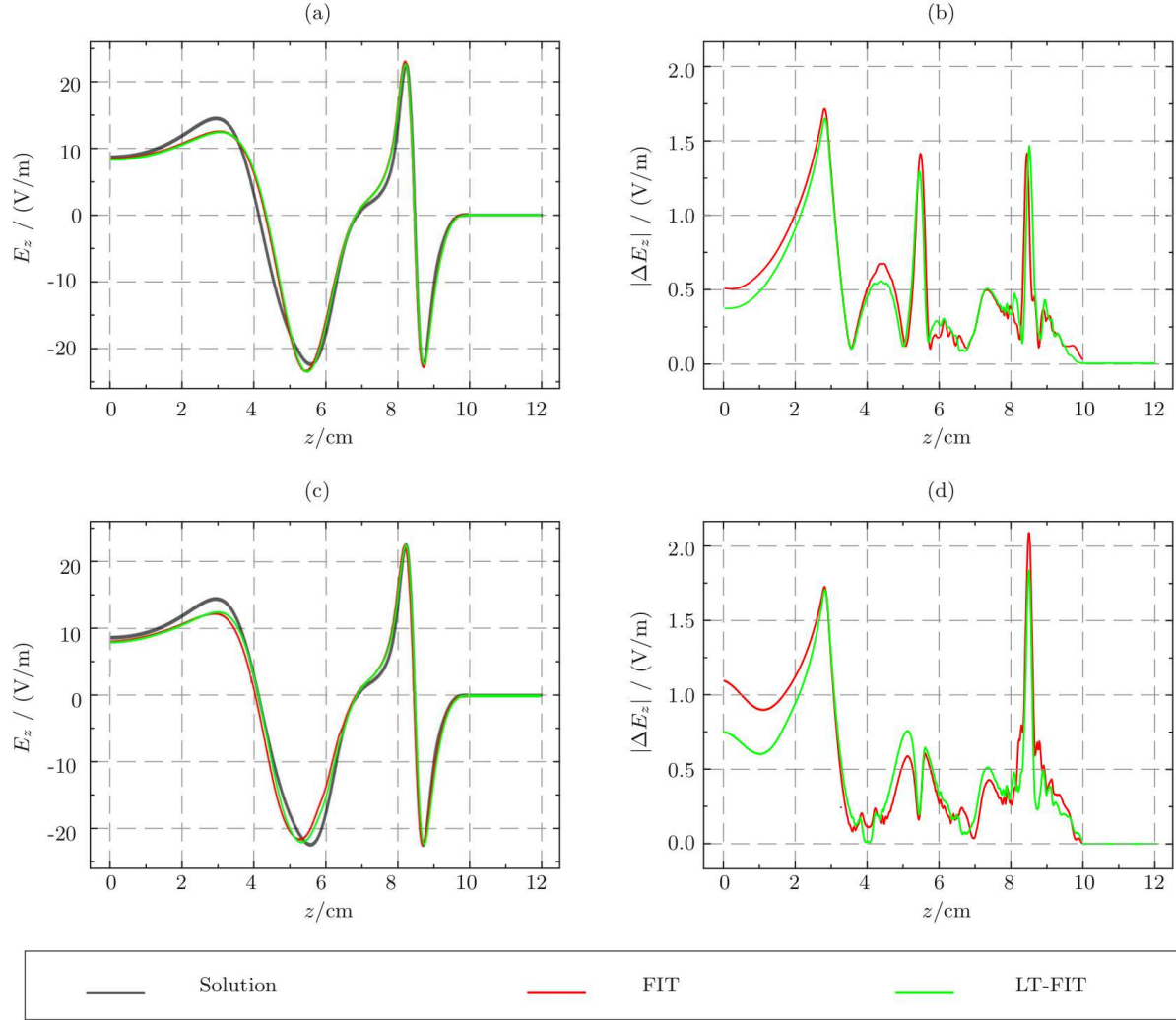


FIG. 10. Longitudinal component of the electric field, excited by a Gaussian bunch traveling in a pipe. The black curve in (a) and (c) indicates the analytical solution for the setup described in Table I. All other curves shows results obtained by the numerical simulation of the problem. In the top row, a static, equidistant computational grid was applied. The results are shown in (a), their errors in (b). In the bottom row, time-adaptive grid refinement ($L = 3$) was applied. In (c) the results for this case are shown and the errors in (d).

nonadaptive grid, which has been employed. For comparability, the settings were chosen such that all simulations finish within less than one hour.

A comparison of the results shows that:

- The relative errors of the FIT and the LT-FIT are similar, however, the TV of the LT-FIT solution is significantly lower, indicating reduced oscillations due to better

numerical dispersion properties.

- For identical numbers of DoF the LT-FIT simulations take longer because of the higher computational costs for the time integration.
- For identical mesh resolutions in the bunch area the adaptive simulations yield errors similar to those obtained on nonadaptive meshes. This follows from a comparison of the result of the adaptive simulations with the respective nonadaptive simulation. Hence, the accuracy of the solutions for this example is mainly determined by the resolution in the bunch region.

B. Self-consistent simulation of the PITZ RF gun

In order to drive a free-electron-laser (FEL) operating by the self-amplified spontaneous-emission (SASE) principle, highly charged electron beams of high brightness are required [23]. The aim of the PITZ project (Photo Injector Test Facility at DESY Zeuthen) [24] is the development and testing of an injector capable of delivering such high quality beams. The injectors for the *Free Electron Laser in Hamburg* (FLASH) [25] and the future *European X-Ray Laser Project* XFEL [26] are under development at PITZ.

The layout of the radio-frequency (RF) gun of the injector is shown in Fig. 11. The emitted bunch is accelerated in a 1.5-cell L-band cavity providing for an accelerating gradient of 42 MV/m at an operational frequency of 1.3 GHz. A focusing technique proposed in [27] is applied in order to compensate for the correlated part of the space charge induced emittance growth. The initial gun layout was designed such that a minimum of the transverse emittance is expected at a distance of approximately 1.6 m downstream of the cathode. At this position a RF cavity is installed in order to accelerate the electrons to relativistic energies. The main design parameters are listed in Table IV.

Many numerical studies of the injector using PIC codes have been performed over the last years. Results have been published, e.g., in [28–32]. However, these simulations either assumed a rotationally symmetric geometry and made use of a so-called 2.5-dimensional approach as implemented in the MAFIA TS2 module [33], or otherwise very short distances in the cm-range of the full three-dimensional model were simulated. Results of parallelized simulations of the full three-dimensional model up to one meter downstream of the cathode

TABLE IV. PITZ design parameters

Parameter	Design value
Bunch charge	1 nC
Transverse laser profile	Hat-profile
Laser spot radius	1 mm
Longitudinal laser profile	Flat-top
Laser pulse duration	22 ps
Rise/Fall time	2 ps
Accelerating gradient	42 MV/m
Transverse emittance	1 mm mrad

have been presented in [4, 34]. However, the exact position of the transverse emittance minimum is required for the optimal placement of the accelerating cavity. Also, the value of the emittance at this position is of strong interest in order to check whether the design value is met.

In the context of this work, the gun was simulated up to a distance of two meters downstream of the cathode. First, settings of the simulation parameter such as the grid resolution and the number of macro particles have been determined. Then, a design study was performed, which addresses the effects of individual injector elements on the beam quality.

Previous investigations have shown that the length of the simulated bunches critically depends on the longitudinal grid step size [35]. In [28] it was stated that a grid resolution of 20 μm longitudinally is required in order to obtain accurate results. In the Fig. 12(a) the results of a parameter study addressing the relation of the longitudinal grid step size and the computed bunch length are presented. The initial 2.5 cm of the gun were simulated using an equidistant grid of 2.5 μm to 80 μm step size. The computed RMS bunch length σ_z at $z = 2.5$ cm varies from 2.24 mm to 2.35 mm. Changing the step size from 5 μm to 2.5 μm results in a variation of σ_z by approximately 1 μm . The computed bunch lengths for a step size of 2.5 μm and 10 μm differ by approximately 10 μm . A longitudinal grid step of 10 μm is considered to be a reasonable balance of computational costs and accuracy.

After emission the electrons have a very low energy of ≈ 5 eV and space charge forces have a strong influence. Since the particles gain energy quickly, it is sufficient to apply the smallest

grid step size only in the immediate vicinity of the cathode. Hence, an additional static grid refinement is applied in this area. In the Fig. 12(b) results for this approach are shown. A grid with a uniform step size of $80 \mu\text{m}$ is statically refined within the first centimeter from the cathode. Refinement levels from one to four have been applied, resulting in step sizes of $40, 20, 10,$ and $5 \mu\text{m}$ within the refined region. The results are, except for minor discrepancies, identical to those obtained with an equidistant grid of the same minimum step size.

For the simulation of the full structure, a combination of static and dynamic mesh refinement was applied providing for a longitudinal resolution of $10 \mu\text{m}$ for the first cm from the cathode and $80 \mu\text{m}$ thereafter. The requirements on the transverse grid step size are less demanding. The width of the simulated bunches using a step size of $2.5 \mu\text{m}$ and $80 \mu\text{m}$ differ by less than $5 \mu\text{m}$. Deviations in the μm -range correspond to some per mille of the bunch width. Choosing a minimum transverse step size of $80 \mu\text{m}$ and a refinement level of five, we obtained an adaptive computational mesh consisting of an average of approximately 82 million cells. A nonadaptive mesh providing for the same minimum resolution would consist of approximately 1.7 billion cells. The bunches in the simulations comprised approximately 0.5 million macro particles.

The results given in the following were obtained with the LT-FIT method. In Fig. 13, the evolution of the horizontal root-mean-square (RMS) bunch width σ_x (a), the RMS bunch length σ_z (b), the average particle energy (c), and the horizontal emittance ε_x (d) for the model shown in Fig. 11 are plotted. The projected emittances ε_x and ε_y are given by $\varepsilon_u = (\sigma_u^2 \cdot \sigma_{p_u}^2 - (\sigma_{u,p_u})^2)^{1/2}$, $u \in \{x, y\}$, where $\sigma_{p_u}^2$ is the momentum variance and σ_{u,p_u} is the covariance of position and momentum.

We performed a design study of the injector in order to identify the individual effects of the diagnostics section, the laser mirror, and the shutter valve on the beam quality in terms of emittance growth. The respective models are shown in the Figs. 14(a)-(d). For each model, an additional element is added. The colors of the curves in Fig. 14(e)-(f) correspond to the outline color of the respective model.

For the model given in Fig. 14(a), the horizontal and vertical emittances, ε_x and ε_y , are identical. This is expected since the geometry is rotationally symmetric for all parts close to the beam. The RF input coupler is obviously not rotationally symmetric but this symmetry violation is hidden by the coupling antenna. In Fig. 14(b), the large opening on

the bottom side of the doublecross introduces an asymmetry of the geometry in horizontal and vertical direction. While ε_x is almost unchanged, the value of ε_y increases by approximately 0.04 mm mrad. The laser mirror, added in the horizontal plane, introduces another asymmetry in Fig. 14(c). An influence on the transverse emittances can be identified in the results but the actual emittance growth at the position of the minimum is small. Finally, the shutter valve depicted in Fig. 14(d) results in significant changes of the transverse emittances. While the horizontal emittance actually decreases by approximately 0.1 mm mrad, the vertical emittance increases by about 0.18 mm mrad in comparison to the structure of Fig. 14(a). Hence, the shutter valve causes a distinct asymmetry in the transverse beam dynamics. In the meantime, a shutter valve with RF shieldings has been installed.

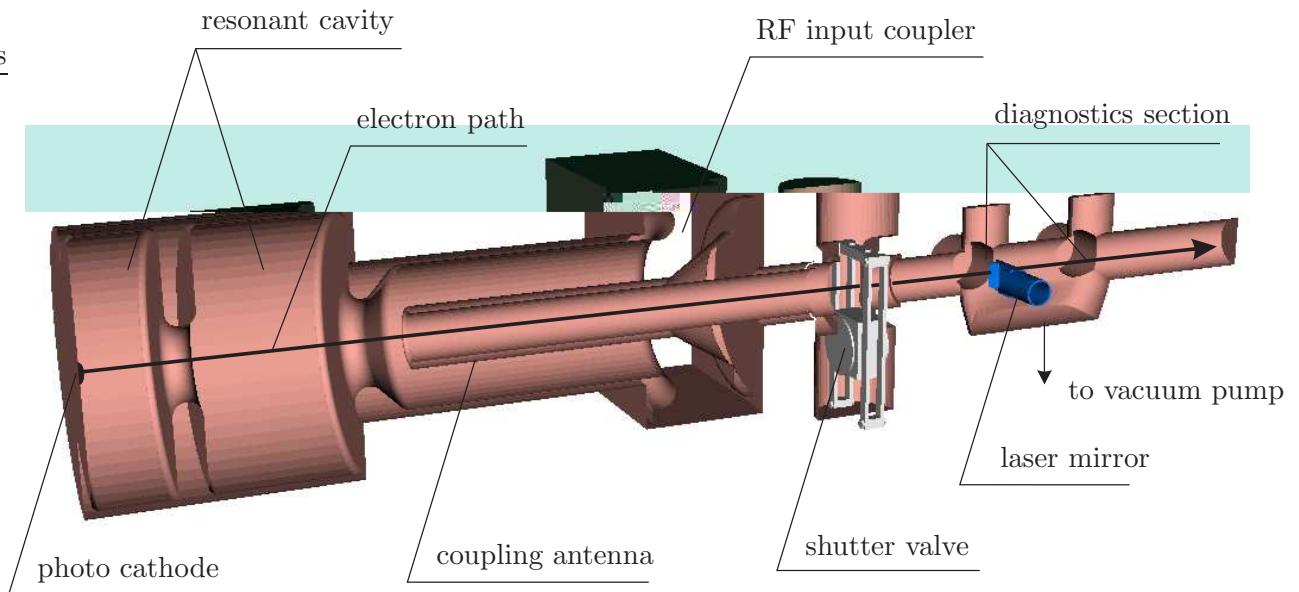


FIG. 11. A CAD model of the injector section of the *Free-electron LASer in Hamburg* (FLASH) is shown in cut view. The depicted part corresponds to approximately 60 cm of the injector. In total 2 m have been modeled. However, the non-depicted part consists only of the beam pipe. A short laser pulse is directed onto the photo cathode, where electrons are emitted. The bunch of electrons is accelerated by a high-frequency electromagnetic field, which is excited in the resonant cavity. It propagates along the electron path through the coupling antenna and passes the shutter valve and the laser mirror, which is inserted through one arm of the diagnostics section. The other arms are used for inserting measurement devices. The opening on its bottom side is connected to a vacuum pump.

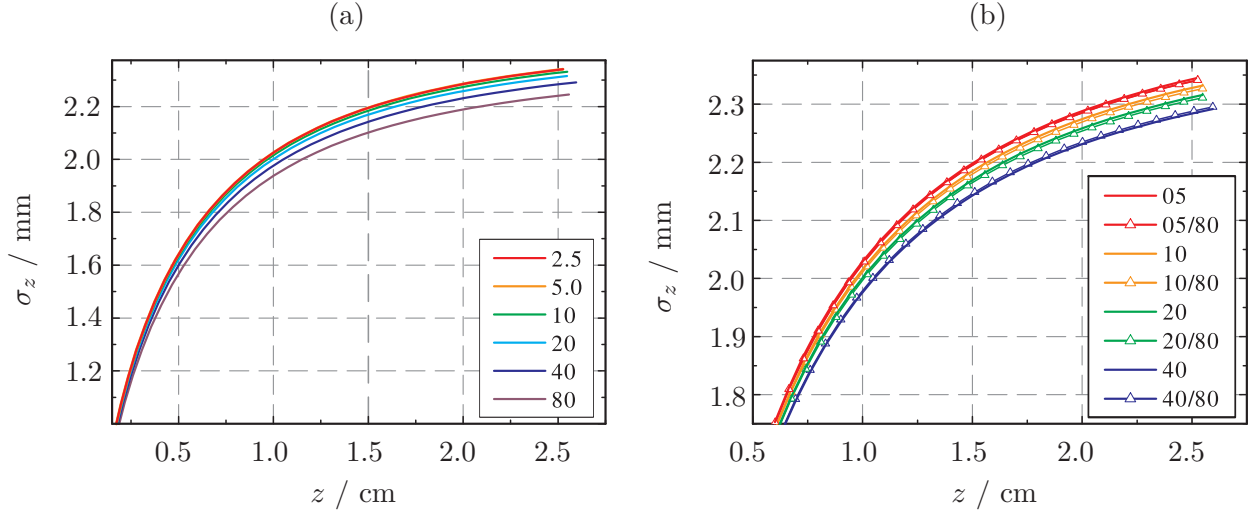


FIG. 12. Computed RMS bunch length vs. longitudinal grid step size. In (a) equidistant grids with different grid step sizes were used. In (b) the equidistant grid with a step size of 80 μm was statically refined within the first cm from the cathode. The step sizes given in the legend are in units of μm .

VII. CONCLUSIONS

In this paper, we extended the framework of Finite Integration Technique to include dynamic mesh refinement. This offers computability on workstations for a class of multi-scale problems, which before was accessible to massively parallelized computations only. In particular, our approach enabled us to perform fully self-consistent simulations of the PITZ RF gun up to two meters downstream from the cathode. We elaborated on the details concerning the mesh refinement and coarsening procedures and presented a novel type of sub-spline interpolation, which is entirely devoid of overshooting. Finally, we performed a design study, which identifies the emittance growth due to individual parts of the gun.

ACKNOWLEDGMENTS

The work of S. Schnepf is supported by the 'Initiative for Excellence' of the German Federal and State Governments and the Graduate School of Computational Engineering at Technische Universität Darmstadt. The authors thank Thomas Lau for providing the

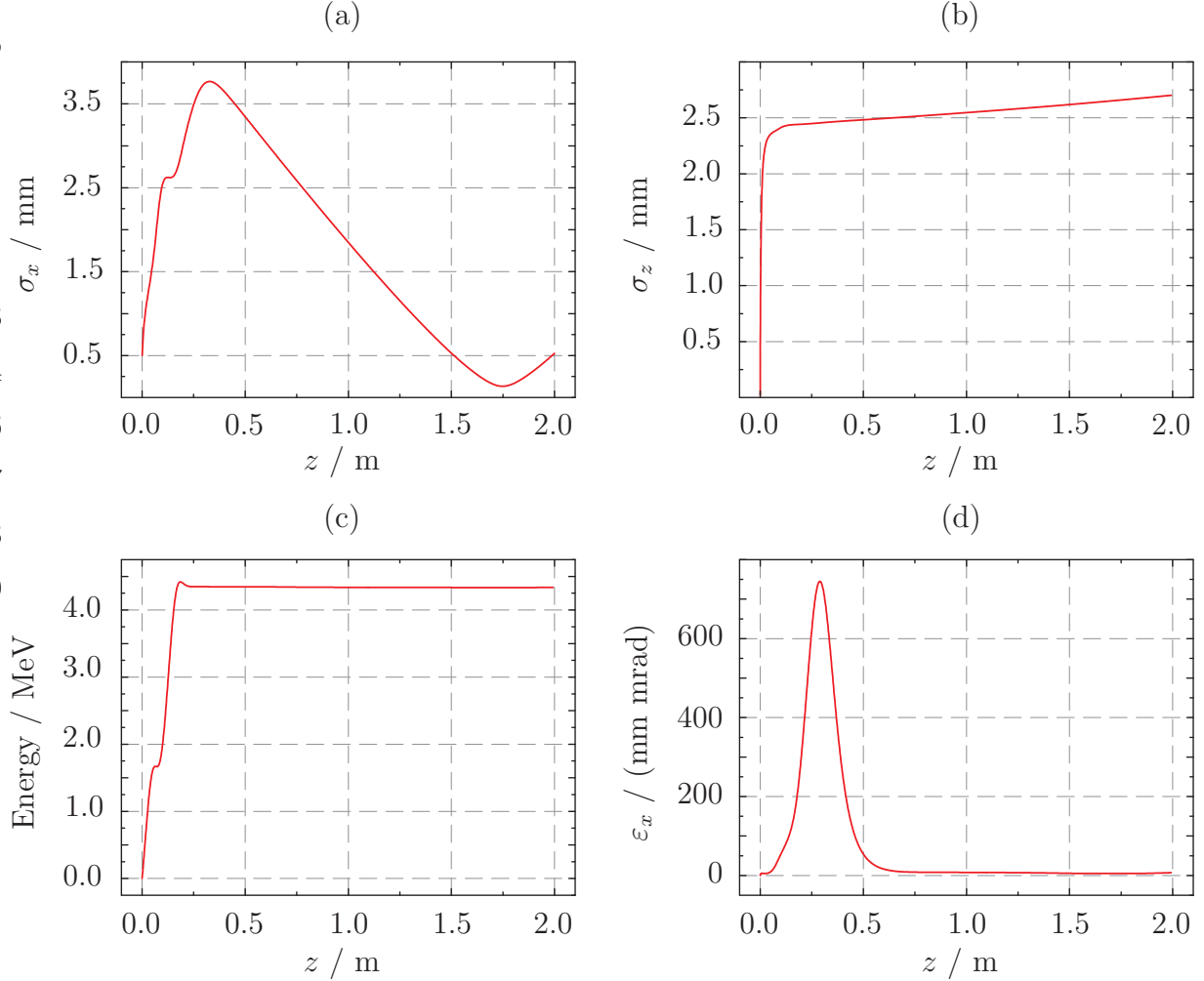


FIG. 13. The plots show the evolution of the RMS bunch width (a), RMS bunch length (b), average particle energy (c), and horizontal emittance (d) along the longitudinal coordinate of the PITZ RF gun.

analytical solution to the example used in Sec. VI A.

-
- [1] F. Wolfheimer, E. Gjonaj, and T. Weiland, Nuclear Instruments and Methods in Physics Research Section A.
 - [2] C. K. Birdsall, *Plasma physics via computer simulation* (Institute of Physics, London, 1991).
 - [3] T. Weiland, Particle Accelerators **15**, 245 (1984).
 - [4] E. Gjonaj, T. Lau, S. Schnepf, F. Wolfheimer, and T. Weiland, New Journal of Physics **8**, 1 (2006).

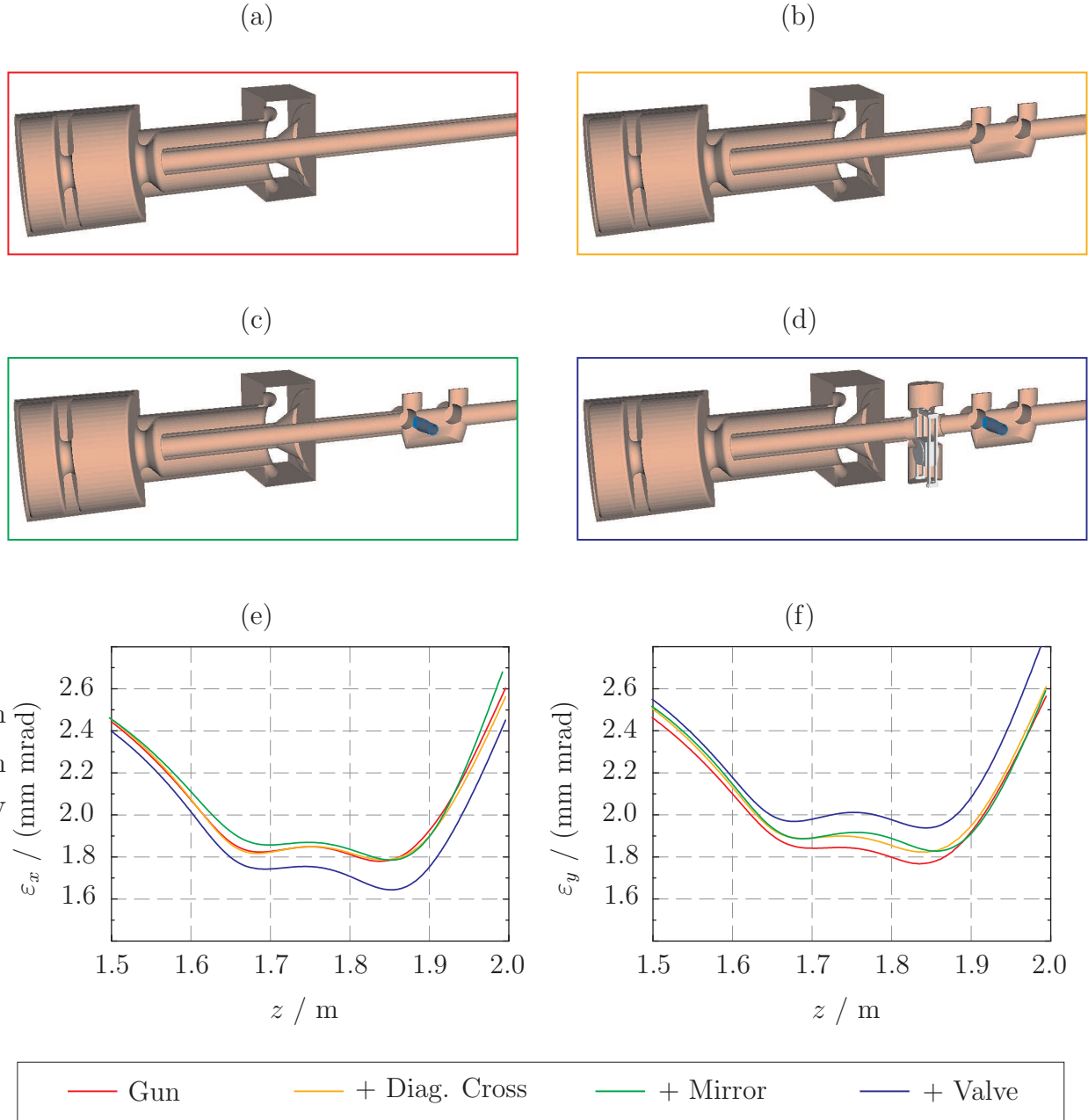


FIG. 14. Models and results of the PITZ RF gun design study. In (a) to (d) the CAD models of the simulated structures are shown. The horizontal and vertical emittances around the position of their minimum are plotted in (e) and (f) respectively. The colors of the curves correspond to the outline color of the models above. While ε_x and ε_y are similar for the case (a), they show a distinct asymmetry for the model depicted in (d).

- [5] T. Weiland, *Particle Accelerators* **17**, 227 (1985).
- [6] G. Strang, *SIAM J. Numerical Analysis* **5**, 506 (1968).
- [7] T. Lau, E. Gjonaj, and T. Weiland, *Zeitschrift für Telekommunikation (FREQUENZ)* **59**, 210 (2005).
- [8] C. Runge, *Zeitschrift für Mathematik und Physik* **46**, 224 (1901).
- [9] C. de Boor, *A Practical Guide to Splines* (Springer, 2001).
- [10] H. Akima, *Jour. ACM* **17**, 589 (1970).
- [11] B. Van Leer, “Lectures notes in physics,” (Springer, 1973) Chap. Towards the ultimate conservative scheme I. The Quest of Monotonicity, pp. 163–168.
- [12] R. J. LeVeque, *Numerical Methods for Conservation Laws* (Birkhäuser, 1990).
- [13] R. Schuhmann and T. Weiland, *Progress in Electromagnetic Research (PIER)* **32**, 301 (2001).
- [14] F. Edelvik, R. Schuhmann, and T. Weiland, *Int. Journal of Numerical Modelling: Electronic Networks, Devices and Fields* **17**, 407 (2004).
- [15] W. Bialowons, M. Bieler, H.-D. Bremer, F.-J. Decker, H.-C. Lewin, P. Schütt, G.-A. Voss, R. Wanzenberg, and T. Weiland, in *Proc. of the 1st European Particle Accelerator Conference (EPAC)*, Vol. 1 (1988) pp. 902–904.
- [16] C. K. Birdsall, *IEEE Trans. Plasma Science* **19**, 65 (1991).
- [17] J. Boris, in *Proc. 4th Conf. Numer. Simulation of Plasmas* (1970).
- [18] C. K. Birdsall and D. Fuss, *Journal of Computational Physics* **3**, 494 (1968).
- [19] J. Villasenor and O. Buneman, *Comput. Phys. Comm.* **69**, 306 (1992).
- [20] I. N. Onishchenko, D. Y. Sidorenko, and G. V. Sotnikov, *Phys. Rev. E* **65** (2002).
- [21] A. Harten, *J. Comp. Phys.* **49**, 357 (1983).
- [22] C. B. Laney, *Computational Gasdynamics* (Cambridge University Press, 1998).
- [23] Z. Huang and K.-J. Kim, *PRST-AB* **10** (2007).
- [24] F. Stephan, K. Abrahamyan, G. Asova, J. Bähr, G. Dimitrov, U. Gensch, H.-J. Grabosch, J. Han, M. Krassilnikov, D. Lipka, V. Miltchev, A. Oppelt, B. Petrosyan, D. Pose, S. Riemann, L. Staykov, M. von Hartrott, E. Jaeschke, D. Krämer, C. Richter, I. Bohnet, J.-P. Carneiro, K. Flöttmann, S. Schreiber, J. Rossbach, P. Michelato, L. Monaco, C. Pagani, D. Sertore, I. Tsakov, W. Sandner, I. Will, W. Ackermann, W. Müller, S. Schnepf, S. Setzer, and T. Weiland, in *Proceedings of the 26th International Free Electron Laser Conference* (2004) pp. 347–350.

- [25] W. Ackermann, G. Asova, V. Ayvazyan, A. Azima, N. Baboi, J. Bähr, V. Balandin, B. Beutner, A. Brandt, A. Bolzmann, R. Brinkmann, O. I. Brovko, M. Castellano, P. Castro, L. Catani, E. Chiadroni, S. Choroba, A. Cianchi, J. T. Costello, D. Cubaynes, J. Dardis, W. Decking, H. Delsim-Hashemi, A. Delserieys, G. D. Pirro, M. Dohlus, S. Düsterer, A. Eckhardt, H. T. Edwards, B. Faatz, J. Feldhaus, K. Flöttmann, J. Frisch, L. Fröhlich, T. Garvey, U. Gensch, C. Gerth, M. Görler, N. Golubeva, H.-J. Grabosch, M. Grecki, O. Grimm, K. Hacker, U. Hahn, J. H. Han, K. Honkavaara, T. Hott, M. Hüning, Y. Ivanisenko, E. Jaeschke, W. Jalmuzna, T. Jezynski, R. Kammering, V. Katalev, K. Kavanagh, E. T. Kennedy, S. Khodyachykh, K. Klose, V. Kocharyan, M. Körfer, M. Kollwe, W. Koprek, S. Korepanov, D. Kostin, M. Krassilnikov, G. Kube, M. Kuhlmann, C. L. S. Lewis, L. Lilje, T. Limberg, D. Lipka, F. Löhl, H. Luna, M. Luong, M. Martins, M. Meyer, P. Michelato, V. Miltchev, W. D. Möller, L. Monaco, W. F. O. Müller, O. Napieralski, O. Napoly, P. Nicolosi, D. Nölle, T. Nuñez, A. Oppelt, C. Pagani, R. Paparella, N. Pchalek, J. Pedregosa-Gutierrez, B. Petersen, B. Petrosyan, G. Petrosyan, L. Petrosyan, J. Pflüger, E. Plönjes, L. Poletto, K. Pozniak, E. Prat, D. Proch, P. Pucyk, P. Radcliffe, H. Redlin, K. Rehlich, M. Richter, M. Roehrs, J. Roensch, R. Romaniuk, M. Ross, J. Rossbach, V. Rybnikov, M. Sachwitz, E. L. Saldin, W. Sandner, H. Schlarb, B. Schmidt, M. Schmitz, P. Schmäuser, J. R. Schneider, E. A. Schneidmiller, S. Schnepp, S. Schreiber, M. Seidel, D. Sertore, A. V. Shabunov, C. Simon, S. Simrock, E. Sombrowski, A. A. Sorokin, P. Spanknebel, R. Spesyvtsev, L. Staykov, B. Steffen, F. Stephan, F. Stulle, H. Thom, K. Tiedtke, M. Tischer, S. Toleikis, R. Treusch, D. Trines, I. Tsakov, E. Vogel, T. W. H. Weise, M. Wellhöfer, M. Wendt, I. Will, A. Winter, K. Wittenburg, W. Wurth, P. Yeates, M. V. Yurkov, I. Zagorodnov, and K. Zapfe, *Nature Photonics* **1**, 336 (2007).
- [26] M. Altarelli, R. Brinkmann, M. Chergui, W. Decking, B. Dobson, S. Düsterer, G. Grübel, W. Graeff, H. Graafsma, J. Hajdu, J. Marangos, J. Pflüger, H. Redlin, D. Riley, I. Robinson, J. Rossbach, A. Schwarz, K. Tiedtke, T. Tschentscher, I. Vartaniants, H. Wabnitz, H. Weise, R. Wichmann, K. Witte, A. Wolf, M. Wulff, and M. Yurkov, *The European X-Ray Free-Electron Laser – Technical design report* (2007).
- [27] B. Carlston, *NIM A* **285**, 313 (1989).
- [28] M. Zhang and P. Schuett, in *Proc. Comp. Acc. Phys. Conf. (CAP)* (1996).

- [29] R. Cee, M. Krassilnikov, S. Setzer, T. Weiland, and A. Novokhatski, *Nucl. Inst. and M. Phys. A* **483**, 321 (2002).
- [30] S. Setzer, W. Ackermann, S. Schnepp, and T. Weiland, in *Proceedings of the 9th European Particle Accelerator Conference* (2004) pp. 1981–1983.
- [31] S. Schnepp, E. Gjonaj, and T. Weiland, in *Proc. 10th European Particle Accelerator Conference (EPAC)* (2006) pp. 2182–2184.
- [32] S. Schnepp, E. Gjonaj, and T. Weiland, in *Proceedings of the 2007 Particle Accelerator Conference* (2007).
- [33] CST GmbH, Bad Nauheimer Str. 19, 64289 Darmstadt, Germany.
- [34] F. Wolfheimer, E. Gjonaj, and T. Weiland, in *Proc. of the 9th Int. Comp. Acc. Phys. Conf. (ICAP)* (2006).
- [35] S. Schnepp, E. Gjonaj, and T. Weiland, in *Proceedings of the 9th International Computational Accelerator Physics Conference* (2006).